ADVANCED FUNCTIONAL MATERIALS
www.afm-journal.de

Thermo-Optically Designed Scalable Photonic Films with High Thermal Conductivity for Subambient and Above-Ambient Radiative Cooling

Pengli Li, Ao Wang, Junjie Fan, Qi Kang, Pingkai Jiang, Hua Bao, and Xingyi Huang**

Radiative cooling is a promising passive cooling technology that reflects sunlight and emits heat to deep space without any energy consumption. Current research mainly focuses on cooling non-heat-generating objects (e.g., water) to a deep subambient temperature under sunlight. Toward real-world applications, however, cooling outdoor objects that generate tremendous heat and have a temperature higher than ambient (e.g., communication base stations and data centres) remains a challenge. Herein, a scalable photonic film is prepared by introducing 2D dielectric nanoplates with high backward scattering efficiency into a polymer using a simulation aided thermo-optical design. It is demonstrated that the dielectric nanoplates can break the trade-off between optical reflection and thermal dissipation of conventional radiative coolers. The photonic film exhibits superior solar reflectance (98%) and has a stronger heat dissipation ability compared to the matrix. It exhibits ≈4 °C subambient cooling performance under direct sunlight and ≈9 °C cooling performance at night. Moreover, it also demonstrates remarkable above-ambient cooling performance by reducing the underlying heater temperature of ≈18 °C in comparison with traditional polymers under sunlight. The dielectric nanoplates reported here provide an innovative strategy for applications related to light management beyond subambient and above-ambient radiative cooling.

1. Introduction

Cooling is in high demand for outdoor applications, such as, for buildings,[1] vehicles,[2] and communication base stations.[3] However, traditional cooling methods (e.g., air conditioners) further aggravate greenhouse gas emissions by consuming ≈10% of global electricity just for building cooling.[4] This vicious circle hinders the sustainable development of our planet. Radiative cooling can dissipate heat into outer space through the atmospheric window (8–13 μm) spontaneously without any energy consumption or CO_2 release, which is the Earth's main self-cooling route.[5] Nocturnal radiative cooling has been utilized since ancient times.[6] In the daytime, however, a few percent absorbances of solar radiation (≈1000 W m^{-2}) can exceed the cooling power and heat any exposed objects.[6b] To reduce heat gain during daytime usually requires the surface to exhibit ultra-high reflectance in the solar spectrum (0.3–2.5 μm).[7] Recently, many researchers have realized daytime subambient radiative cooling through designing spectrally selective photonic structures with high reflectance in the solar spectrum and high emittance in the atmospheric window.[1a,b,7a,8] It can cool the surface of a non-heat-generating object (usually a metal plate) to a temperature lower than ambient under direct sunlight.

Although current spectrally selective photonic structures allow us to obtain valuable cold sources to cool non-heat-generating objects to subambient temperatures for refrigeration applications such as food storage,[7b] in many other practical applications with high cooling demand, such as, data centres,[9] vehicles,[2] and communication base stations,[3] the objects subjected to cooling usually have higher temperatures than ambient owing to tremendous internal heat generation (i.e., above-ambient cooling).[2] Therefore, designing a photonic structure that works for both subambient and above-ambient radiative cooling is highly desirable and can greatly extend the potential applications of this energy-saving cooling technology.

Whether for subambient or above-ambient radiative cooling, the photonic structure should have high thermal emittance in the atmospheric transparent window (8–13 μm) to transfer excess heat to the cold deep space. Generally, subambient radiative cooling prefers the photonic structure with thermal emittance selectively in the atmospheric transparent window, because the selective photonic structure can suppress parasitic heat absorption from the atmosphere.[8c] The suppressed parasitic heat absorption endows the selective photonic structure with lower stagnation temperature than the broadband photonic structure below ambient as shown in **Figure 1**a,b and Note S3, Supporting Information. Toward practical applications

P. Li, Q. Kang, P. Jiang, X. Huang
Department of Polymer Science and Engineering
Shanghai Key Laboratory of Electrical Insulation and Thermal Aging
The State Key Laboratory of Metal Matrix Nanocomposites
Shanghai Jiao Tong University
Shanghai 200240, P. R. China
E-mail: xyhuang@sjtu.edu.cn

A. Wang, J. Fan, H. Bao
University of Michigan-Shanghai Jiao Tong University Joint Institute
Shanghai Jiao Tong University
Shanghai 200240, P. R. China
E-mail: hua.bao@sjtu.edu.cn

The ORCID identification number(s) for the author(s) of this article can be found under https://doi.org/10.1002/adfm.202109542.

DOI: 10.1002/adfm.202109542

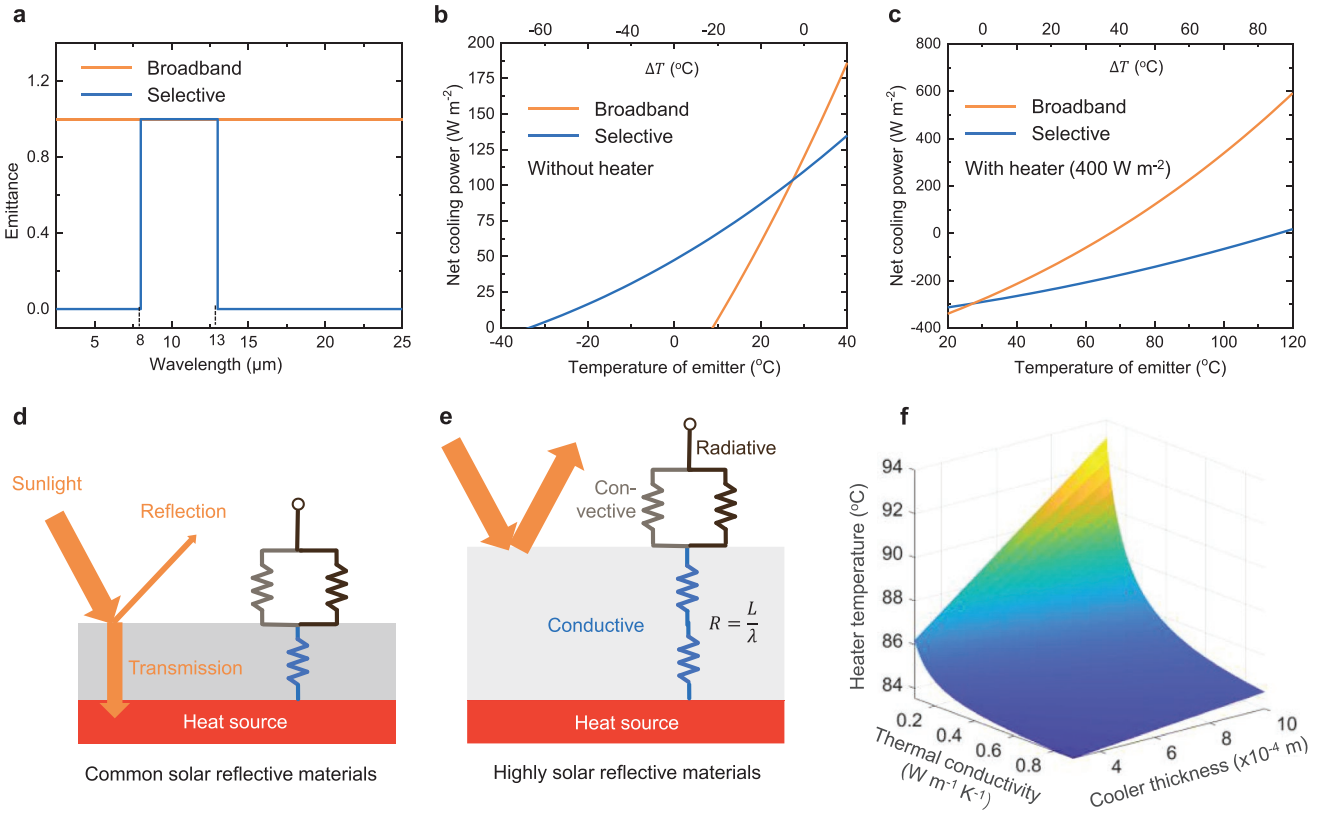

Figure 1. a) Spectrum of broadband and selective emitter used in the calculations. b) Calculated net cooling power for subambient radiative cooling as a function of emitter temperature. c) Calculated net cooling power for above-ambient radiative cooling as a function of emitter temperature. The calculation set non-radiative heat transfer coefficient $h_c = 0$. d) Schematic of low solar reflective photonic structures. e) Schematic of highly solar reflective photonic structures. Increasing the solar heat reflectivity requires a greater thickness L, which also increases the thermal resistance of the photonic structure and thus makes it unfavourable for heat dissipation. f) Simulated temperature of the underneath heat source as a function of thermal resistance of the radiative cooler. In the calculation, a heat flux of 1000 W m^{-2} without sunlight was assumed.

of subambient radiative cooling, however, the objects subject to cooling usually have large thermal capacity and can only be cooled to a temperature slightly lower or close to ambient. In this case, from Figure 1b, one can see that the broadband phonic structure exhibit larger cooling power than the selective one. When considering above-ambient radiative cooling applications with large heat generation (Figure 1c), because of the additional heat exchange with the atmosphere, the broadband photonic structure has an extra cooling channel and shows much larger cooling power.[10] Therefore, broadband emittance is preferred when pursuing a balanced cooling effect for subambient and above-ambient radiative cooling abilities.

For above-ambient cooling, in addition to broadband infrared emittance and high solar reflectance, the photonic structure itself should also have a low thermal resistance ($R = L/\lambda$, where L is thickness and λ is thermal conductivity) to dissipate large heat flux (Figure 1d,e). However, such a requirement has seldom been addressed in previous photonic structures development. For example, high solar reflectance is generally achieved by multiple light scattering in hybrid photonic structures,[8b,c,11] composed of a low thermal conductivity polymer matrix (e.g., <0.4 W m^{-1} K^{-1})[12] and light scatterers, such as, dielectric particles (SiO_2, $BaSO_4$, $CaCO_3$, etc.),[11b–f,13] or pores.[8b,c,11g,h,13,14] These commonly used light scatterers have low efficiency due to low refractive index, forward scattering, and coherent scattering. Therefore, it requires a large number of scattering events to reverse the direction of the incident light, which is usually achieved by increasing the thickness (L) of photonic structures. On the other hand, the vast majority of photonic structures have low thermal conductivity (λ) and are usually used for heat insulation.[11a] These factors eventually lead to the photonic structures having high thermal resistances (R). The effect of radiative cooling may be suppressed or even cancelled out by the high thermal resistance and thus cause heat accumulation (Figure 1f). Therefore, designing a photonic structure that works for both subambient and above-ambient radiative cooling remains a huge scientific challenge. An additional noble metal solar reflective layer such as silver[8a,15] may reduce thermal resistance by reducing the thickness needed, but this requires complex preparation procedures and is susceptible to corrosion.

In this study, based on theoretical guidance for the photonic structure's design that accounts for both subambient and above-ambient radiative cooling, we report a scalable photonic film based on 2D hexagonal boron nitride (h-BN) dielectric nanoplates filled with a polymer matrix. Combining a unique 2D shape with a high refractive index, the h-BN has an ultra-high backward light scattering efficiency that enables the photonic

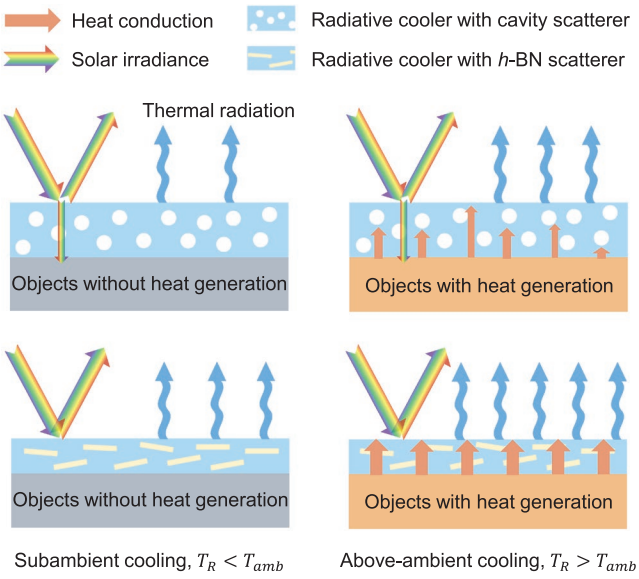

Figure 2. Schematic comparison of radiative coolers with cavity or *h*-BN scatterer. Cavity scatterer hinders heat dissipation in above-ambient radiative cooling while *h*-BN scatterer promotes this process. Besides, *h*-BN scatterer can achieve higher solar reflectance than the spherical one.

film with high solar reflectance and a low thermal resistance simultaneously (**Figure 2**). The photonic film exhibits excellent subambient radiative cooling performance that is comparable to that of state-of-the-art photonic structures. More importantly, at above-ambient radiative cooling conditions, it exhibits a much better cooling effect than conventional photonic structures. It also possesses flame retardancy, outdoor durability, electrical insulation, and flexibility that fit practical radiative cooling application requirements.

2. Results and Discussion

2.1. Thermal-Optically Designing a Multifunctional Photonic Structure

To design a photonic structure that works for both subambient and above-ambient radiative cooling, it should have both high solar reflectance and low thermal resistance. The high solar reflectance of a photonic structure is usually achieved by multiple scattering of sunlight. This is made by introducing numerous interfaces with dielectric contrast. The interfaces can be created by introducing pores or another dielectric particle in a polymer matrix with a different refractive index.[11e] As pores significantly increase the thermal resistance of the photonic structure, they cannot be used for above-ambient radiative cooling.[11a,16] In this case, dielectric contrast can be achieved by introducing micro- or nano dielectric particles with sizes comparable to the solar wavelength in the polymer matrix (**Figure 3**a–c). A candidate dielectric particle should have a larger band gap than the energy of solar photons (0.49–4.13 eV) to avoid sunlight absorbance.[17] Moreover, a higher refractive index particle is more favorable, because a large dielectric contrast with the matrix leads to stronger scattering of individual particles, resulting in greater reflection.

A wide band gap generally leads to a low refractive index.[17,18] Existing dielectric particles, such as, SiO_2, Al_2O_3, and $BaSO_4$ have a very wide band gap (≈9, 8.8, and 7.6 eV, respectively). Their refractive indexes (≈1.46, 1.78, and 1.64, respectively, at 500-µm wavelength) do not have a high enough contrast with that (≈1.5) of the polymer matrix, resulting in low scattering efficiency. A high loading is usually needed to increase the number of scattering events. Besides, optical crowding occurs at high loading as a result of coherent scattering, which further reduces the scattering efficiency of the dielectric particles.[19] Therefore, a large photonic structure thickness is usually required to achieve ultra-high solar reflectance.

In contrast, ultra-high-refractive-index particles, such as TiO_2 (whose index is ≈2.56 at 500-µm wavelength), can achieve higher reflectance in the visible and near-infrared wavelength range than the same amount of other dielectric particles.[11b,20] However, its use causes considerable absorption in the ultraviolet (UV) wavelength range because of its narrow band gap of 3.0 eV, which limits the solar reflectance of TiO_2-based paints to <92%.[11b,e] Based on the above theoretical analysis, we can narrow the range of choice for dielectric particles with band gaps larger than but close to the upper limit of solar photons (4.13 eV). The band gap, refractive index, and thermal conductivity of commonly used dielectric particles are summarized in Figures S1 and S2, Supporting Information. Among the various particles, we found that *h*-BN best fits our selection principles, while it has not yet been elucidated in the literature. The restriction of electron delocalization in the π bonds of *h*-BN endows it with a relatively wide band gap (5.96 eV) than the energy of solar photons.[21] On the other hand, its band gap is not as large as that of Al_2O_3 and $BaSO_4$, resulting in a higher refractive index of 2.2 at a wavelength of 500 µm[22] (Figures S1 and S2, Supporting Information).

In particular, *h*-BN has a unique 2D shape. The shape of the particles significantly affects the direction in which the light is scattered (usually defined as asymmetry factor, *g*). We expect the deflection angle of the scattered light to be as large as possible, preferably backward (smaller *g*). Because this would reduce the number of scattering events needed to reverse the incident light. We adopted the discrete dipole approximation (DDA) method to obtain the scattering coefficient and asymmetry factor of 2D particles and spherical particles.[23] From the DDA calculation results in Figure 3d,e one can see that although spherical particles have a larger scattering coefficient, they also have a much larger asymmetry factor than 2D particles. This means that most of the light scattered by spherical particles continues in the forward direction with only a little deviation from its original direction (Figure 3g,h). In contrast, the scattering of 2D particles is more isotropic and has larger backward components (Figure 3i,j and Figures S3 and S4, Supporting Information). Combining the scattering coefficient with asymmetry factor in Figure 3f, we use angle-weighted scattering coefficient (σ = scattering coefficient × (1 − *g*)) to quantificationally compare the backward scattering efficiency between 2D particles and spherical particles. Obviously, 2D particles have a larger angle-weighted scattering coefficient, which means they allow more light to scatter backward. Moreover, when

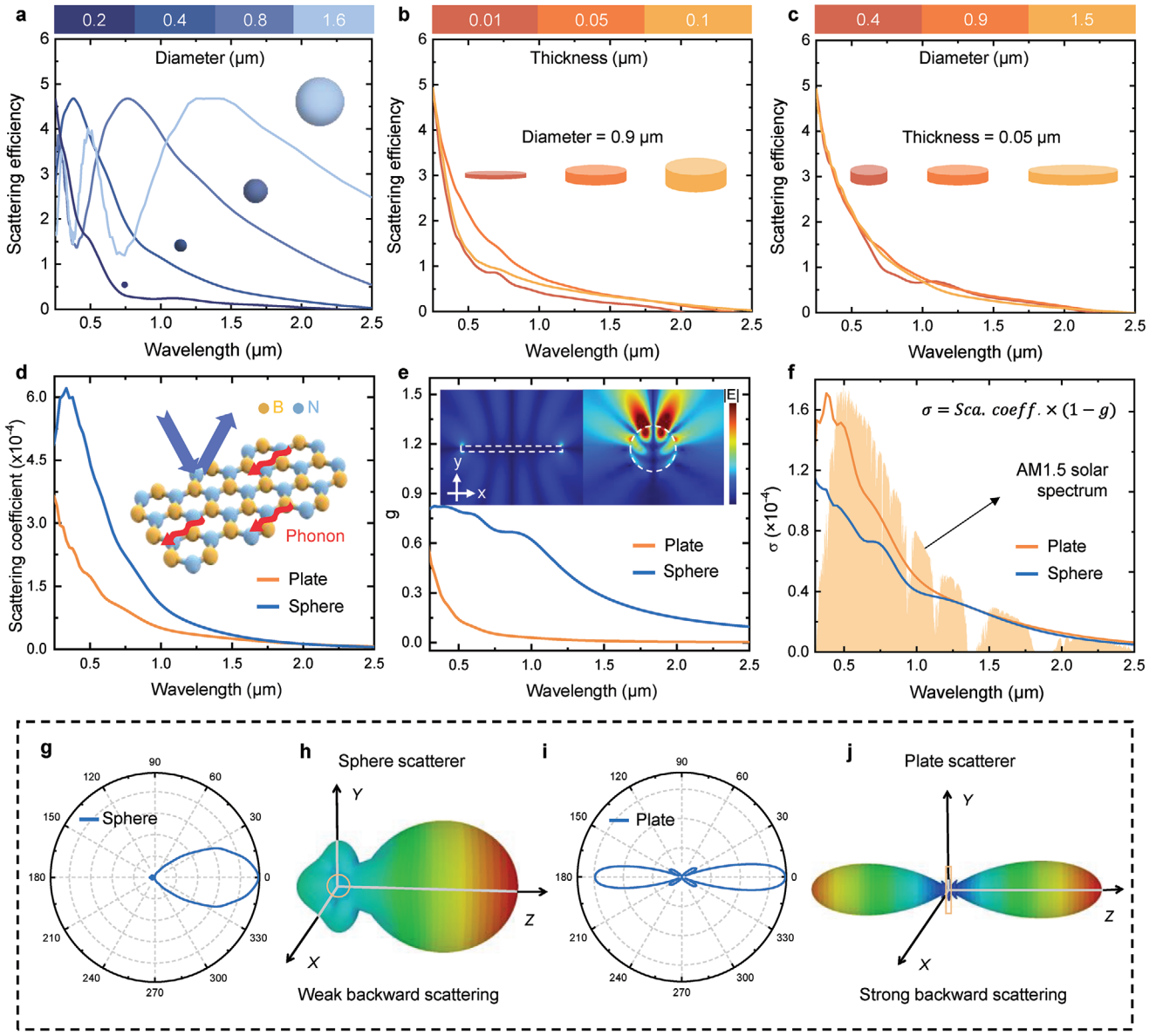

Figure 3. Optical properties comparison between plate and sphere scatterer. a) Calculated scattering efficiencies for spheric scatterers with different sizes. b) Calculated scattering efficiencies for 2D scatterers with the same diameter but different thickness. c) Calculated scattering efficiencies for 2D scatterers with the same thickness but different diameters. d) Scattering coefficient of a plate (diameter = 0.9 μm, thickness = 0.05 μm, and refractive index = 2) and a sphere (of the volume as the plate, with diameter = 0.39 μm and refractive index = 2). The inset shows the schematic of *h*-BN. e) Light scattering asymmetry factor (*g*) of the plate and sphere in (d). The inset shows the electric field distributions of the plate and sphere, both with the same refractive index, illuminated at 0.4-μm wavelength. f) Angle-weighted scattering coefficient (σ) of the plate and sphere in (d). g) Polarization diagram of the sphere with 0.5-μm wavelength illumination. h) 3D far-field scattering pattern of the sphere with 0.5-μm wavelength illumination. i) Polarization diagram of the plate with 0.5-μm wavelength illumination. j) 3D far-field scattering pattern of the plate with 0.5-μm wavelength illumination.

combining with a higher refractive index, 2D particles can have a much larger backward scattering efficiency (Figure S5a–c, Supporting Information).

We then adopted the Monte Carlo method to evaluate the reflection property of the hybrid photonic structures, using the scattering efficiency and asymmetry factor of the DDA simulation. As Figure S5d, Supporting Information, shows, 2D particles with a refractive index of 2 gave a high solar reflectance of 96.8%, whereas spherical particles with an index of 1.6 can only obtain a reflectance of 86.7%. It should be noted that 86.7% solar reflectance is in general insufficient to achieve daytime subambient radiative cooling, unless at very dry atmospheric conditions.

As a proof of concept, the DDA simulation (Figures S6 and S7, Supporting Information) and experiments (Figure S8, Supporting Information) were conducted for *h*-BN and other commonly used dielectric particles. The simulation and experiments all prove that the *h*-BN can bring much higher backward scattering efficiency and solar reflectance for the photonic films.

In addition to unprecedented optical properties, *h*-BN also has a very high thermal conductivity (>400 W m^{-1} K^{-1}), which

can further reduce the thermal resistances of the hybrid photonic structures.[24] Therefore, based on our theoretical analysis and numerical simulations, we identified *h*-BN as an ideal light scatterer to fabricate hybrid photonic structures with both subambient and above-ambient radiative cooling abilities.

2.2. Large-Scale Production of Photonic Films

We introduced 2D *h*-BN nanoplates randomly into a polydimethylsiloxane (PDMS) polymer matrix. PDMS has a low extinction coefficient in the solar spectrum but has five main extinction coefficient peaks between 8 and 13 µm, making it a type of low-solar-absorption but high-infrared-emission polymer (Figure S9, Supporting Information). The size of the *h*-BN nanoplate is concentrated between 600 and 1200 nm (Figure S10a,b, Supporting Information), which is close to the size used in our simulation (900 nm). We then manufactured a meter-long white photonic film (**Figure 4**a) through a scalable, high-efficiency, low-cost hot-pressing method, which is an ordinary processing method widely used in laboratories and factories. Because of its simple structure, this photonic film can also be prepared using other continuous processing methods for industrial-scale manufacturing.

The dispersion of the scatterer is an important factor in determining the optical and thermal properties of the photonic film. It can be seen from Figure 4b and Figure S10c,d, Supporting Information, that *h*-BN nanoplates are generally uniformly dispersed and most are aligned along the film plane. This is conducive to creating abundant dielectric contrast interfaces for light scattering. We fabricated a series of photonic films with different thicknesses and scatterer loadings. The solar reflectance of the photonic films first increases rapidly with the increase in thickness and scatterer loading and then increases slowly when approaching the reflectance limits (Figure S11, Supporting Information). When the volume fraction of the scatterer is 40.5%, the photonic film exhibits a high reflectivity of 98% in the 0.3–2.5 µm wavelength range and a high infrared (IR) emissivity of 0.89 (90.3% in the 8–13 µm atmospheric window) (Figure 4c). Besides, the reflectivity has little dependence on the angle (Figure S12, Supporting Information). This indicates that the photonic film can quite diffusively reflect sunlight. In previous studies, however, reaching such a high level of solar reflectivity by use of other dielectric particles, such as $BaSO_4$ or $CaCO_3$, generally requires scatterer loading of 60–92 vol% (Table S1, Supporting Information).[11b,e]

Heat conduction pathways can be formed in the photonic film with 40.5 vol% *h*-BN nanoplates (Figure S13a, Supporting Information), which increase the phonon mean free path in the photonic film.[25] The in-plane thermal conductivity of the photonic film exceeds 3 W m^{-1} K^{-1} (Figure S13b, Supporting Information), while the through-plane thermal conductivity achieves 1.3 W m^{-1} K^{-1} (Figure 4d), which is much higher than that (≈0.18 W m^{-1} K^{-1}) of the PDMS matrix and photonic films

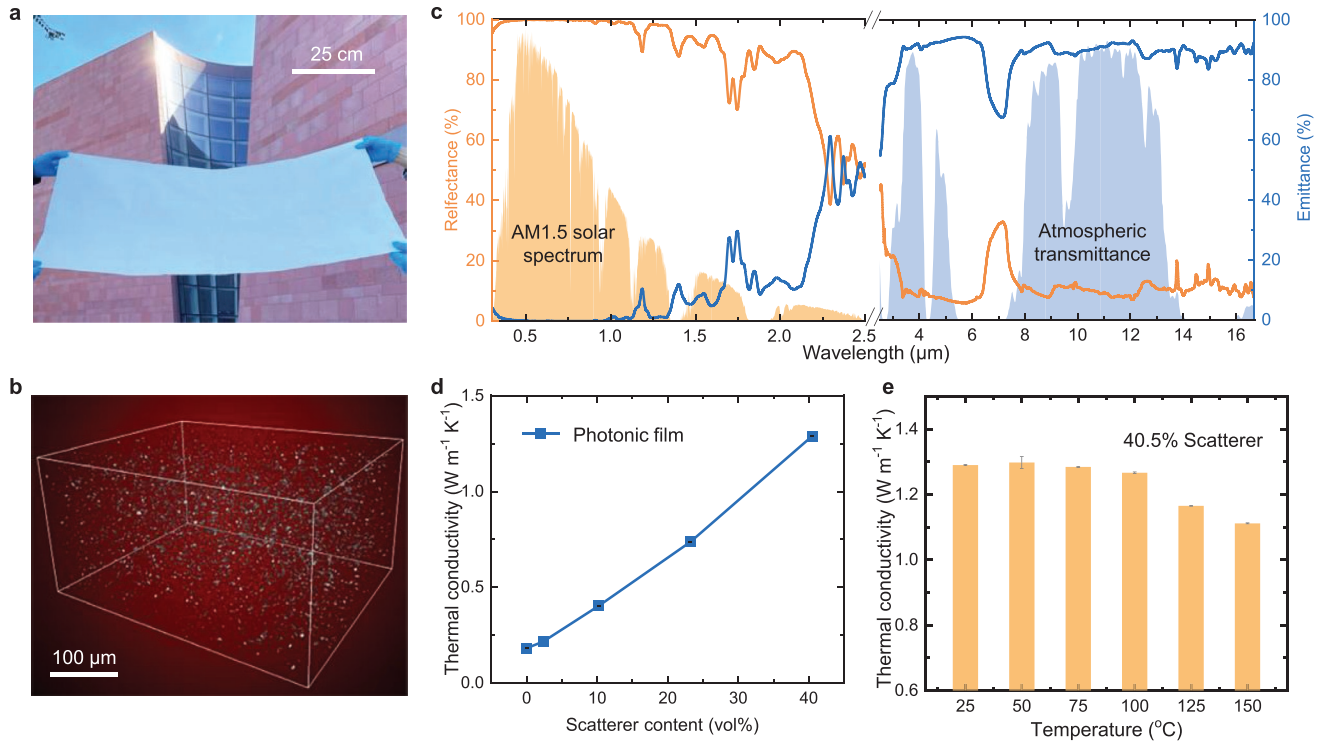

Figure 4. Optical and thermal properties of the photonic film. a) Photograph of the photonic film with an area of 100 × 50 cm^2 produced by hot pressing. b) 3D image of the distribution of *h*-BN nanoplate in the 40.5 vol% photonic film characterized by micro-X-ray computed tomography. c) Reflectance and emissivity of a 1.4-mm-thick photonic film at UV–vis–IR wavelengths against AM1.5 solar spectra and the atmospheric window. d) Thermal conductivity of photonic film as a function of scatterer content. e) Dependence of the thermal conductivity of photonic film on temperature in the range of 25–150 °C. The error bars represent the standard deviation over three independent measurements at different regions of the samples.

filled with other scatterers (Figures S8i and S14, Supporting Information). This photonic film not only has low thermal resistance in the through-plane direction but also can spread the hot-spot heat rapidly.[26] Considering the comprehensive optical, thermal, and mechanical properties of the photonic film, we set the scatterer content to 40.5 vol% for the subsequent experiments.

For above-ambient radiative cooling applications, it is expected that the photonic film can work at high temperatures. In this case, the thermal dissipation property of the photonic films should preferably be independent of temperature. For example, it can be seen from Figure 4e that the thermal conductivity of the photonic film is scarcely reduced below 100 °C. Besides, the thermal emittance is also stable as the temperature increases to 200 °C (Figure S15, Supporting Information). Moreover, it also has great thermal stability, which exhibits no weight loss below 330 °C (Figure S16, Supporting Information) and has an excellent flame retardancy[27] (Figure S17, Supporting Information). This is important for the fire safety of buildings and electronic products.[27]

2.3. All-Day Subambient Radiative Cooling

It is expected that the photonic film we designed has outstanding all-day subambient radiative cooling performance comparable to that of traditional photonic structures. We conducted a three-day outdoor experiment to demonstrate the subambient radiative cooling property of the photonic film. The outdoor experimental apparatus we used is shown in **Figure 5**a,b. The sample with a thermocouple and an aluminum plate beneath was placed on a polystyrene foam insulation sample holder, which was then placed inside an acrylic (poly(methyl methacrylate)) box and covered with a polyethylene IR-transparent wind shield, similar to the experimental setup reported previously.[15,28] An ambient temperature thermocouple was placed in the Stevenson screen to prevent heating by sunlight but still allow sufficient natural convection to measure a more accurate ambient temperature[11f] (Figure S18a, Supporting Information). A pyranometer and a hygrometer were used to measure the solar intensity and relative humidity, respectively, in real time (Figure 5d). It has been reported that in high-humidity areas, water molecules in the atmosphere absorb the IR radiation and thus impede the heat exchange between the Earth and deep space.[29] Our photonic film exhibited high-performance continuous subambient radiative cooling even in coastal cities with high relative humidity (Figure 5c,d). The photonic film achieved a 4 °C subambient cooling effect and a cooling power of 63 W m^{-2} under the highest solar intensity of ≈700 W m^{-2} at noon (Figure 5d,e and Figure S18b–d, Supporting Information). The average subambient cooling temperature at 48 h was 7.3 °C. This experiment demonstrates that the scalable photonic film exhibits prominent all-day subambient cooling properties.

2.4. High-Performance Above-Ambient Radiative Cooling

In addition to excellent subambient radiative cooling performance, to demonstrate its above-ambient cooling performance, we designed the experimental device shown in the inset of **Figure 6**a. A silicone rubber heater was used to simulate the heated electronics. Indoor experiments were first performed to exclude the variable of solar reflectance. We compared the photonic film with higher thermal IR emittance (0.92) but high

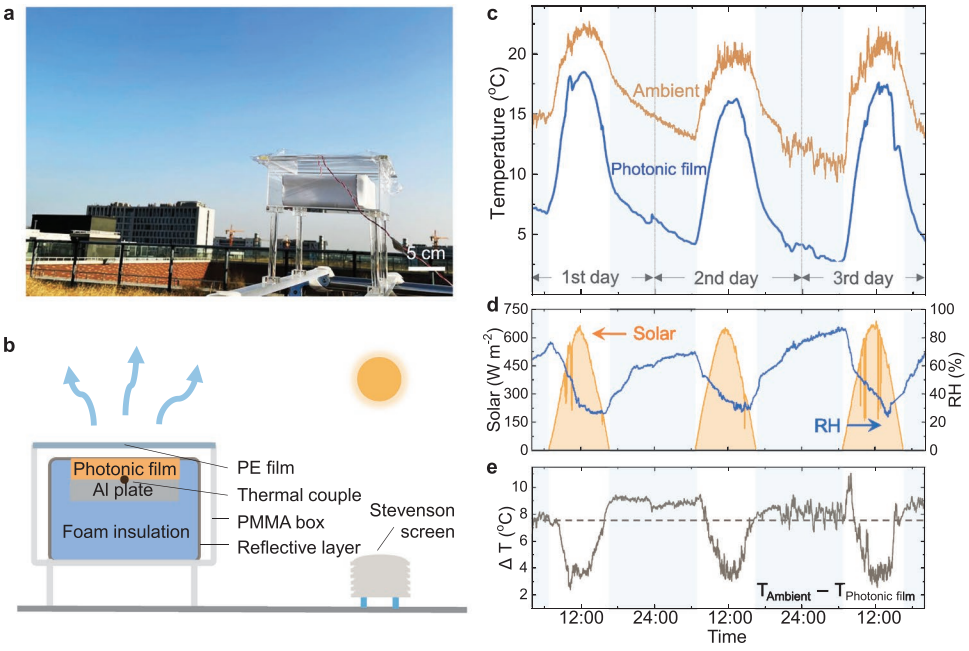

Figure 5. Continuous subambient radiative cooling. a) Photograph of subambient radiative cooling measurement setup. b) Schematic of the measurement setup. c) Real-time temperatures of ambient air and the photonic film in the outdoor experiment. The experiment lasted for 3 days. d) Real-time recorded solar intensity and relative humidity (RH) in the outdoor experiment. e) Real-time temperature differences between ambient air and the photonic film in the outdoor experiment. The dashed line is the average temperature difference for 48 h.

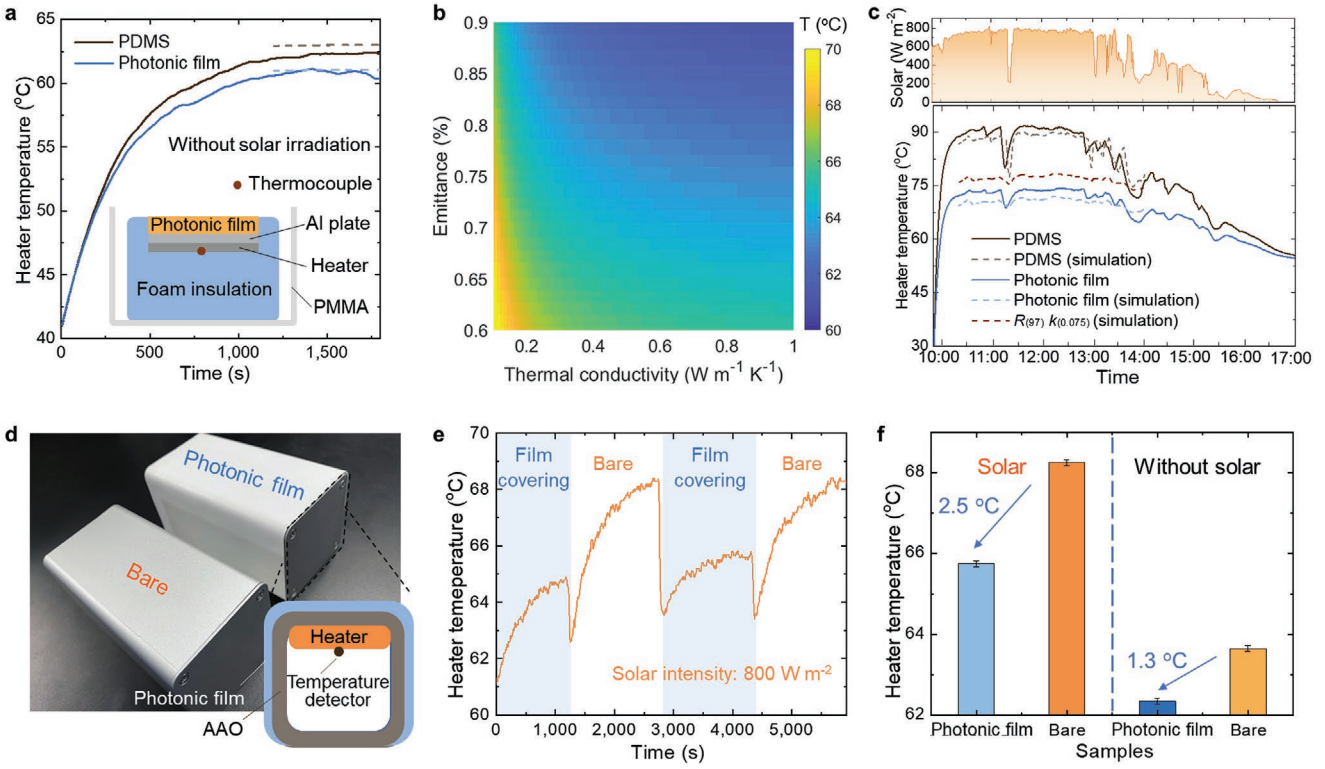

Figure 6. Above-ambient radiative cooling. a) Measured heater temperature covered by 1-mm-thick high-thermal-resistance (PDMS) and photonic film. The inset shows the setup of experiment. The dashed line shows the calculation results. b) Temperature of the heater in (a) as a function of thermal conductivity and emittance of photonic film. The calculation parameter is based on the experimental results in (a). c) Measured solar intensity (top) and the heater temperature (bottom) covered by different materials. The experimental parameters are the same as those of (a). The dashed line shows the calculation results. d) Experimental setup showing the electronic equipment with a heater inside. e) Temperature tracking for the heater in an AAO box covered and with 1 mm of photonic film peeled off several times under simulated sunlight. f) Equilibrium temperature of the heater in covered and bare AAO boxes with and without solar irradiation. The error bars represent the standard deviation over two cycles of tests.

thermal resistance PDMS (λ = 0.18 W m^{-1} K^{-1}) to explore the significant role of thermal resistance. With an internal heat generation power of 700 W m^{-2}, the photonic film exhibited excellent cooling performance compared to that of PDMS, as it reached a temperature drop of 2 °C below that of PDMS, which was also verified by thermal simulation (see the dotted line in Figure 6a). Then, we extended the simulation to a wider emittance and thermal resistance range and found that thermal resistance is an important limiting factor for radiative cooling apart from thermal emittance (Figure 6b). Thus, it can be inferred that the cooling effect of our photonic film is more prominent than that of porous solar reflective radiative coolers (mostly heat insulators). On the other hand, one can observe improved cooling performance under a higher heat flux. For example, under a heat flux of 2000 W m^{-2}, the heater experienced a cooling of 14.3 °C when covered with different thermal resistance materials ($T_{\lambda = 0.1\ \mathrm{W\ m^{-1}\ K^{-1}}} - T_{\lambda = 2\ \mathrm{W\ m^{-1}\ K^{-1}}}$), whereas the temperature drop was 5.0 °C when the heating power was 700 W m^{-2} (Figure S19, Supporting Information).

We next performed a continuous outdoor experiment to simulate the real application scenarios of outdoor objects that need to bear the exterior solar heat load and interior heat generation at the same time. Similarly, a 10-µm-thick polyethylene film was used as the wind shield, and the real-time ambient temperature and relative humidity were recorded (Figure S20, Supporting Information). Under the peak solar intensity of near 800 W m^{-2}, the photonic film brings an ≈18 °C temperature drop compared to PDMS (whose total solar reflectivity of 61% is achieved by a white heat-conducting tape and silicone rubber heater underneath) (Figure 6c). This significant temperature reduction proves the importance of high solar reflectance for high-performance above-ambient radiative cooling of the outdoor devices. At night, when there was no solar radiation, our photonic film still has a lower temperature than PDMS, which demonstrates the significant impact of thermal resistance (Figure S21, Supporting Information). To demonstrate the superior above-ambient radiative cooling capacities of the photonic film to traditional radiative cooling materials, we calculated the temperature of a hypothetical radiative cooler with a high solar reflectance of 97% and a thermal conductivity of 0.075 W m^{-1} K^{-1} (detail in Note S2, Supporting Information). One can see that in Figure 6c, the photonic film has an ≈7 °C temperature drop compared to the hypothetical radiative cooler at noon, confirming its excellent above-ambient cooling capabilities.

To demonstrate the convenience of using this photonic film, we performed a model experiment. We found that simply covering the photonic film on the anodized alumina (AAO) packaging box can help the trapped heat to escape and block the input of solar heat (Figure 6d). We repeatedly pasted and peeled

off the photonic film to investigate the equilibrium temperature change of the heater. Although the AAO we used already has an excellent above-ambient cooling ability with a solar reflectance of 82% and an IR emittance of 0.82, the AAO box covered by the photonic film still experienced a 2.5 °C temperature drop under 800 W m^{-2} simulated sunlight and a 1.3 °C drop even without a solar load (Figure 6e,f and Figure S22, Supporting Information). These experiments prove that the photonic film is viable for the efficient above-ambient radiative cooling of outdoor objects.

2.5. Toward Practical Applications

It is worth noting that our scalable manufactured photonic film has uniform high qualities (Figure S23, Supporting Information). For outdoor applications, the durability of the photonic film for long-term use is important. As shown in Figure S24, Supporting Information, after 30-day outdoor tests, the solar reflectance of the photonic films decreased by 0.35% and thermal emittance decreased by 2.2%. While after 72-h UV-accelerated ageing tests, the solar reflectance of the photonic films decreased by 0.4% but thermal emittance increased by 1.1%.

Additionally, instead of decreasing, the thermal emission of the photonic film increases after abrasion test because of the reduction of impedance mismatch (Figure S25, Supporting Information). This property is important for application areas exposed to sandstorms. We tested the dielectric constant and dielectric loss of the photonic film at 1 MHz between 20 and 140 °C (Figure S26, Supporting Information). This photonic film has a low dielectric constant of <4 and gradually decreases as the temperature rises, which is vital for not interfering with signal propagation. This photonic film also maintains a dielectric loss at the 10^{-3} level in the test temperature range. A low dielectric loss is required for high-voltage applications, as a high dielectric loss will change the high-frequency alternating current to heat and may cause thermal breakdown of the material. In addition, this low-filler-loading photonic film also has excellent flexibility and thus is suitable for covering curved surfaces (Figure S27, Supporting Information). To satisfy different application requirements, *h*-BN nanoplate can also be mixed with other polymer matrices, such as, poly(vinylidene fluoride-hexafluoropropylene) to produce paint-like photonic structures. This paint can be used to coat the surface of different materials, such as, glass and wood (Figure S28, Supporting Information).

3. Conclusions

In summary, this study offers a fundamental insight into the application of 2D dielectric nanoplates in radiative cooling. Accordingly, 2D *h*-BN scatterer with a wide band gap, high refractive index, and high backward scattering efficiency was introduced into flexible matrix to fabricate a scalable photonic film, which has excellent subambient radiative cooling performance on par with state-of-the-art photonic structures. More importantly, it exhibits unprecedented heat dissipation and solar heat shielding properties for above-ambient radiative cooling. In addition to their unprecedented cooling ability, large-scale production photonic films also exhibit numerous essential practical properties (e.g., fire resistance, outdoor aging resistance, electrical insulation, and flexibility) and can be instantly adopted for the efficient cooling of residential and industrial applications. We expect that the 2D dielectric nanoplates reported here will revolutionize the related light and thermal management field beyond radiative cooling.

4. Experimental Section

Preparation of the Photonic Film: The *h*-BN filler (3M Technical Ceramics, USA) was added to PDMS precursors (Dow Corning Sylgard 184, USA). Thereafter, ethyl acetate was added as a diluent. The ratio of ethyl acetate to components A and B of the PDMS precursors was 2:10:1. The *h*-BN/PDMS precursor/ethyl acetate was then mixed using a planetary mixer (Thinky ARE-250, Japan) at a rotation speed of 2000 rpm for 15 min. Afterward, the mixture was placed in a vacuum oven for over 30 min at ambient temperature. The photonic film was fabricated using the hot-pressing method at a pressure of 10 MPa at 150 °C for 15 min. The thickness of the photonic film was controlled by a custom-made stainless mould.

Sample Characterization: The 3D image of the photonic film was taken by micro-CT microscope (Zeiss Xradia 520 Versa, Germany). A triple ion-beam cutter (Leica Em tic 3x, Germany) was used to polish the cross section of the photonic films. The microstructure images were obtained by scanning electron microscope (FEI Nova NanoSEM 450, USA). XRD patterns were measured by an X-ray diffractometer (Bruker D8 ADVANCE Da Vinci, Germany). Full angle reflection was measured by angle-resolved spectrum system in micro-region (Ideaoptics, China). The reflectance (R) and transmittance (T) were measured using a UV–vis–near IR spectrometer (PerkinElmer Lambda 950, USA) in the range of 0.25–2.5 µm with an integrating sphere in the mid-IR range using a Fourier-transform IR spectrometer (Thermo Scientific Nicolet 6700, USA) with a gold integrating sphere (Pike Technology, USA). The emittance (E) is obtained from the equation $E = 1 - R - T$.

The solar reflectance ($\bar{R}_{solar}$) is defined as

$$\bar{R}_{solar} = \frac{\int_{0.3\,\mu m}^{2.5\,\mu m} I_{solar}(\lambda) \times R_{solar}(\lambda,\theta)\, d\lambda}{\int_{0.3\,\mu m}^{2.5\,\mu m} I_{solar}(\lambda)\, d\lambda} \quad (1)$$

where λ is the wavelength, θ is the angle of incidence of light, $I_{solar}(\lambda)$ is the ASTM G173 global solar intensity spectrum, and $R_{solar}(\lambda,\theta)$ is the angular spectral reflectance of the surface.

The IR emittance ($\bar{E}_{infrared}$) is defined as

$$\bar{E}_{infrared} = \frac{\int_{2.5\,\mu m}^{\infty} I_{BB}(T,\lambda) \times E(T,\lambda)\, d\lambda}{\int_{2.5\,\mu m}^{\infty} I_{BB}(T,\lambda)\, d\lambda} \quad (2)$$

where $I_{BB}(T,\lambda)$ is the emittance spectra of a blackbody at temperature T (here assumed to be 25 °C) and $E(T, \lambda)$ is the spectral hemispherical thermal emittance of the surface.

The IR emittance ($\bar{E}_{8-13\,\mu m}$) within the atmospheric window is defined as

$$\bar{E}_{8-13\,\mu m} = \frac{\int_{8\,\mu m}^{13\,\mu m} I_{BB}(T,\lambda) \times E(T,\lambda)\, d\lambda}{\int_{8\,\mu m}^{13\,\mu m} I_{BB}(T,\lambda)\, d\lambda} \quad (3)$$

Measurement of Thermal Properties: The specific heat (C_p) and thermal diffusivity (α) were measured using the laser flash method (Netzsch LFA 467, Germany), and the density (ρ) was assessed using the water

displacement method. The thermal conductivity (λ) was then calculated from $\lambda = \alpha \times \rho \times C_p$. The thermal stability was measured using a thermogravimetric analyser (Netzsch TG209 F3, Germany) under an air atmosphere at a heating rate of 20 °C min^{-1}.

Measurement of Mechanical Properties: The tensile strength test was performed using a universal test instrument (Instron 3343, USA). The dumbbell-shaped sample was 5 cm long and 0.5 cm wide with a gauge distance of 2 cm. The cross-head speed was 50 mm min^{-1}.

Measurement of Electrical Properties: The temperature-dependent dielectric constant and dielectric loss of the photonic film from 20 to 145 °C were measured using a high-resolution impedance analyzer (GmbH Novocontrol Alpha-N Concept 40, Germany).

Thermal Measurement: The temperatures of the ambient air and the sample were measured using a resistance temperature detector, which was connected to a data acquisition unit (Keysight 34972A, USA) whose resolution was ±0.1 °C. The resistance temperature detector was calibrated before the measurement. Thermal conductive adhesive tape was placed on the back surface of the samples to ensure good thermal contact. For the indoor test, a 500-W xenon lamp (Osram, Germany) was used to simulate solar radiation.

Supporting Information

Supporting Information is available from the Wiley Online Library or from the author.

Acknowledgements

This work was supported by National Natural Science Foundation of China (51877132, 51636004).

Conflict of Interest

The authors declare no conflict of interest.

Data Availability Statement

The data that support the findings of this study are available from the corresponding author upon reasonable request.

Keywords

light scattering, optical simulation, radiative cooling, solar reflection, thermal management, 2D nanoplates

Received: October 3, 2021
Published online: October 20, 2021

[1] a) T. Li, Y. Zhai, S. He, W. Gan, Z. Wei, M. Heidarinejad, D. Dalgo, R. Mi, X. Zhao, J. Song, J. Dai, C. Chen, A. Aili, A. Vellore, A. Martini, R. Yang, J. Srebric, X. Yin, L. Hu, *Science* **2019**, *364*, 760; b) Y. Zhou, H. M. Song, J. W. Liang, M. Singer, M. Zhou, E. Stegenburgs, N. Zhang, C. Xu, T. Ng, Z. F. Yu, B. Ooi, Q. Q. Gan, *Nat. Sustain.* **2019**, *2*, 718; c) R. G. Yang, X. B. Yin, *Nat. Sustain.* **2019**, *2*, 663; d) X. Li, B. Sun, C. Sui, A. Nandi, H. Fang, Y. Peng, G. Tan, P. C. Hsu, *Nat. Commun.* **2020**, *11*, 6101.

[2] S. Y. Heo, G. J. Lee, D. H. Kim, Y. J. Kim, S. Ishii, M. S. Kim, T. J. Seok, B. J. Lee, H. Lee, Y. M. Song, *Sci. Adv.* **2020**, *6*, eabb1906.

[3] Thermal Management Challenges in the 5G Era, https://www.nwengineeringllc.com/article/thermal-management-challenges-in-the-5g-era.php (accessed: May 2021).

[4] Cooling, https://www.iea.org/fuels-and-technologies/cooling (accessed: Jan 2021).

[5] N. N. Shi, C. C. Tsai, F. Camino, G. D. Bernard, N. Yu, R. Wehner, *Science* **2015**, *349*, 298.

[6] a) Z. Chen, L. Zhu, A. Raman, S. Fan, *Nat. Commun.* **2016**, *7*, 13729; b) B. Bhatia, A. Leroy, Y. Shen, L. Zhao, M. Gianello, D. Li, T. Gu, J. Hu, M. Soljacic, E. N. Wang, *Nat. Commun.* **2018**, *9*, 5001.

[7] a) A. P. Raman, M. A. Anoma, L. Zhu, E. Rephaeli, S. Fan, *Nature* **2014**, *515*, 540; b) D. L. Zhao, A. Aili, Y. Zhai, S. Y. Xu, G. Tan, X. B. Yin, R. G. Yang, *Appl. Phys. Rev.* **2019**, *6*, 021306.

[8] a) Y. Zhai, Y. Ma, S. N. David, D. Zhao, R. Lou, G. Tan, R. Yang, X. Yin, *Science* **2017**, *355*, 1062; b) J. Mandal, Y. Fu, A. C. Overvig, M. Jia, K. Sun, N. N. Shi, H. Zhou, X. Xiao, N. Yu, Y. Yang, *Science* **2018**, *362*, 315; c) D. Li, X. Liu, W. Li, Z. Lin, B. Zhu, Z. Li, J. Li, B. Li, S. Fan, J. Xie, J. Zhu, *Nat. Nanotechnol.* **2021**, *16*, 153; d) M. H. Kang, G. J. Lee, J. H. Lee, M. S. Kim, Z. Yan, J. W. Jeong, K. I. Jang, Y. M. Song, *Adv. Sci.* **2021**, *8*, 2004885; e) W. Huang, Y. Chen, Y. Luo, J. Mandal, W. Li, M. Chen, C. C. Tsai, Z. Shan, N. Yu, Y. Yang, *Adv. Funct. Mater.* **2021**, *31*, 2010334; f) W. Gao, Z. Lei, K. Wu, Y. Chen, *Adv. Funct. Mater.* **2021**, *31*, 2100535.

[9] A. S. Fleischer, *Science* **2020**, *370*, 783.

[10] J. Jaramillo-Fernandez, G. L. Whitworth, J. A. Pariente, A. Blanco, P. D. Garcia, C. Lopez, C. M. Sotomayor-Torres, *Small* **2019**, *15*, 1905290.

[11] a) A. Leroy, B. Bhatia, C. C. Kelsall, A. Castillejo-Cuberos, H. M. Di Capua, L. Zhao, L. Zhang, A. M. Guzman, E. N. Wang, *Sci. Adv.* **2019**, *5*, eaat9480; b) J. Mandal, Y. Yang, N. F. Yu, A. P. Raman, *Joule* **2020**, *4*, 1350; c) X. Xue, M. Qiu, Y. Li, Q. M. Zhang, S. Li, Z. Yang, C. Feng, W. Zhang, J. G. Dai, D. Lei, W. Jin, L. Xu, T. Zhang, J. Qin, H. Wang, S. Fan, *Adv. Mater.* **2020**, *32*, 1906751; d) H. Zhang, K. C. S. Ly, X. Liu, Z. Chen, M. Yan, Z. Wu, X. Wang, Y. Zheng, H. Zhou, T. Fan, *Proc. Natl. Acad. Sci. U. S. A.* **2020**, *117*, 14657; e) X. Li, J. Peoples, Z. Huang, Z. Zhao, J. Qiu, X. Ruan, *Cell Rep. Phys. Sci.* **2020**, *1*, 100221; f) S. Atiganyanun, J. B. Plumley, S. J. Han, K. Hsu, J. Cytrynbaum, T. L. Peng, S. M. Han, S. E. Han, *ACS Photonics* **2018**, *5*, 1181; g) T. Wang, Y. Wu, L. Shi, X. Hu, M. Chen, L. Wu, *Nat. Commun.* **2021**, *12*, 365; h) Y. C. Peng, J. Chen, A. Y. Song, P. B. Catrysse, P. C. Hsu, L. L. Cai, B. F. Liu, Y. Y. Zhu, G. M. Zhou, D. S. Wu, H. R. Lee, S. H. Fan, Y. Cui, *Nat. Sustain.* **2018**, *1*, 105.

[12] a) C. Huang, X. Qian, R. Yang, *Mater. Sci. Eng., R* **2018**, *132*, 1; b) X. Y. Huang, C. Y. Zhi, Y. Lin, H. Bao, G. N. Wu, P. K. Jiang, Y. Mai, *Mater. Sci. Eng., R* **2020**, *142*, 100577; c) P.-C. Hsu, C. Liu, A. Y. Song, Z. Zhang, Y. Peng, J. Xie, K. Liu, C.-L. Wu, P. B. Catrysse, L. Cai, S. Zhai, A. Majumdar, S. Fan, Y. Cui, *Sci. Adv.* **2017**, *3*, e1700895.

[13] L. Cai, A. Y. Song, W. Li, P. C. Hsu, D. Lin, P. B. Catrysse, Y. Liu, Y. Peng, J. Chen, H. Wang, J. Xu, A. Yang, S. Fan, Y. Cui, *Adv. Mater.* **2018**, *30*, 1802152.

[14] a) P. C. Hsu, A. Y. Song, P. B. Catrysse, C. Liu, Y. Peng, J. Xie, S. Fan, Y. Cui, *Science* **2016**, *353*, 1019; b) H. Zhao, Q. Sun, J. Zhou, X. Deng, J. Cui, *Adv. Mater.* **2020**, *32*, 2000870; c) X. Wang, X. H. Liu, Z. Y. Li, H. W. Zhang, Z. W. Yang, H. Zhou, T. X. Fan, *Adv. Funct. Mater.* **2020**, *30*, 1907562.

[15] D. L. Zhao, A. Aili, Y. Zhai, J. T. Lu, D. Kidd, G. Tan, X. B. Yin, R. G. Yang, *Joule* **2019**, *3*, 111.

[16] X. Xu, Q. Zhang, M. Hao, Y. Hu, Z. Lin, L. Peng, T. Wang, X. Ren, C. Wang, Z. Zhao, C. Wan, H. Fei, L. Wang, J. Zhu, H. Sun, W. Chen, T. Du, B. Deng, G. J. Cheng, I. Shakir, C. Dames, T. S. Fisher, X. Zhang, H. Li, Y. Huang, X. Duan, *Science* **2019**, *363*, 723.

[17] Z. Tong, J. Peoples, X. Li, X. Yang, H. Bao, X. Ruan, arXiv preprint arXiv:2101.05053, **2021**.

[18] N. M. Ravindra, P. Ganapathy, J. Choi, *Infrared Phys. Technol.* **2007**, *50*, 21.
[19] M. P. Diebold, *Application of Light Scattering to Coatings: A User's Guide*, Springer, Berlin **2014**.
[20] H. Bao, C. Yan, B. Wang, X. Fang, C. Y. Zhao, X. Ruan, *Sol. Energy Mater. Sol. Cells* **2017**, *168*, 78.
[21] a) G. Cassabois, P. Valvin, B. Gil, *Nat. Photonics* **2016**, *10*, 262; b) Q. Li, G. Zhang, F. Liu, K. Han, M. R. Gadinski, C. Xiong, Q. Wang, *Energy Environ. Sci.* **2015**, *8*, 922.
[22] Y. Rah, Y. Jin, S. Kim, K. Yu, *Opt. Lett.* **2019**, *44*, 3797.
[23] B. T. Draine, P. J. Flatau, *J. Opt. Soc. Am. A* **1994**, *11*, 1491.
[24] P. Q. Jiang, X. Qian, R. G. Yang, L. Lindsay, *Phys. Rev. Mater.* **2018**, *2*, 8.
[25] a) H. L. Zhu, Y. Y. Li, Z. Q. Fang, J. J. Xu, F. Y. Cao, J. Y. Wan, C. Preston, B. Yang, L. B. Hu, *ACS Nano* **2014**, *8*, 3606; b) J. Chen, X. Huang, Y. Zhu, P. Jiang, *Adv. Funct. Mater.* **2017**, *27*, 1604754; c) X. Zeng, J. Sun, Y. Yao, R. Sun, J.-B. Xu, C.-P. Wong, *ACS Nano* **2017**, *11*, 5167.
[26] J. Chen, X. Huang, B. Sun, P. Jiang, *ACS Nano* **2019**, *13*, 337.
[27] W. Gan, C. Chen, Z. Wang, Y. Pei, W. Ping, S. Xiao, J. Dai, Y. Yao, S. He, B. Zhao, S. Das, B. Yang, P. B. Sunderland, L. Hu, *Adv. Funct. Mater.* **2020**, *30*, 1909196.
[28] E. A. Goldstein, A. P. Raman, S. H. Fan, *Nat. Energy* **2017**, *2*, 7.
[29] a) C. Liu, Y. Wu, B. Wang, C. Y. Zhao, H. Bao, *Sol. Energy* **2019**, *183*, 218; b) B. Zhao, M. K. Hu, X. Z. Ao, G. Pei, *Appl. Therm. Eng.* **2019**, *155*, 660.